Upscaling vegetation cover from UAV to satellite imagery

Elena Belcore [1], Marco Piras [1], Alvaro Moreno[2], Ana B. Ruescas[2]

[1] DIATI, Department of Environment, Land and Infrastructure Engineering, Politecnico di Torino, Corso Duca degli Abruzzi, 24, 10129 Torino, Italy - elena.belcore@polito.it, marco.piras@polito.it
[2] Image Processing Laboratory (IPL), Universitat de València, Paterna, Spain - ana.b.ruescas@uv.es, alvaro.moreno@uv.es

Keywords: Fractional cover; UAV–satellite upscaling; Vegetation mapping; Dirichlet evidential network; PlanetScope

Abstract

This study proposes an upscaling approach to estimate multi-species fractional cover of coastal dune vegetation by combining UAV-based (Uncrewed Aerial Vehicles) classification and PlanetScope imagery. A thirteen-species classification generated from a UAV multispectral dataset at 3cm spatial resolution was used to derive the Fractional cover (FC) as species composition on PlanetScope dataset. The spectral representativeness and consistency of the FC were tested, and then used as training information for a Dirichlet-based neural network, which provides both predictions and associated uncertainty. The method is tested on three coastal areas (200m along the coast) using a Leave-One-Area-Out (LOAO) validation scheme and then applied along the entire dune system of the Massacciucoli Regional Park (Tuscany, Italy). Results show stable performance across the three LOAO cycles and macro-RMSE values between 0.11 and 0.41. Herbaceous species show relatively low errors, while woody species and the sand background class remain more difficult to model, mainly due to structural complexity and spectral heterogeneity. Specific abundance-corrected metrics were computed to deal with rare species, whose evaluation is affected by near-zero values, showing robust results for most species.

1. Introduction

Mapping vegetation species at the individual level across landscape scales holds significant ecological, landscape, and indirectly geomorphological relevance, given the close relationship between soil stability, erosion processes, and root-system structure. Remote sensing provides the only practical framework for extending such information from local observations to landscape-scale monitoring (Alvarez-Vanhard et al., 2021). In this context, limited to passive optical remote sensing, the dichotomy between UAVs (Uncrewed Aerial Vehicles) and satellites is a recurring theme. Numerous studies have explicitly compared the strengths and limitations of these two optical remote sensing approaches, offering critical insights into their respective capabilities and optimal use (Alvarez-Vanhard et al., 2021).

In vegetation mapping, satellite Earth Observation (EO) systems are well established for large-scale mapping of diverse vegetation and functional types (Räsänen et al., 2019). However, in coastal ecosystem monitoring, the most significant vegetation elements are herbaceous , which directly contribute to dune morphological processes and, consequently, to coastal erosion and deposition. In vegetation dune monitoring, functional groups and types classifications are often insufficient for capturing species-level information, particularly in areas characterized by high biodiversity. However, the spatial resolution of most satellites (e.g., Sentinel, Landsat) is insufficient for accurate species-level detection. Recent availability of commercial high-resolution EO missions (<10 m) is gradually bridging this gap (Alvarez-Vanhard et al., 2021). Nevertheless, even high-resolution satellite data, such as those from the PlanetScope SuperDove constellation, often remain insufficient for reliable species discrimination in complex vegetation mosaics (Karakizi et al., 2024).

The need for high spatial resolution has recently been partially satisfied by multispectral UAVs, which provide very high spatial resolution but limited coverage. Indeed, UAV-mounted multispectral sensors have rapidly expanded in recent years thanks to improved spatial resolution, integration with dual-frequency positioning and irradiance sensors, and relatively affordable cost, opening a new phase of applied UAV-based remote sensing (Alvarez-Vanhard et al., 2021). Vegetation classification from multispectral UAV data using machine learning models has therefore become increasingly frequent, often demonstrating high accuracy at local scale (Agrillo et al., 2023; Belcore et al., 2024). Yet, employing UAVs across extensive areas is often prohibitive due to operational costs, time-consuming acquisition, and intensive processing demands. Moreover, the transferability of UAV-based classification models to larger, heterogeneous contexts is typically limited and seldom evaluated (Alvarez-Vanhard et al., 2021).

In this evolving scenario, the need to bridge the gap between UAV data and satellite observations for producing species-level maps over large areas is evident (Alvarez-Vanhard et al., 2021). A crucial aspect of this integration hypothesis involves the conceptual and methodological alignment between different spatial scales. In this regard, different upscaling strategies have emerged, intending to transfer fine-scale information acquired from UAV platforms to satellite-derived data. Recent studies have demonstrated the effectiveness of such integrative methods in applications that embrace species distribution modelling, phenological monitoring, biomass estimation, and precision agriculture. Relevant examples include invasive species mapping (Kattenborn et al., 2020; Paz-Kagan et al., 2019), biomass and carbon stock estimation (Leitão et al., 2019; Villoslada et al., 2024), vegetation cover assessment (Agrillo et al., 2023; Gessner et al., 2013; Nasiri et al., 2022), plant disease mapping (Yamati et al., 2023), and deadwood detection (Schiefer et al., 2023). Upscaling techniques, in particular, have been widely applied to propagate fine-scale information to broader spatial extents (Leitão et al., 2019; Villoslada et al., 2024).

A key concept in these multiscale approaches is fractional cover (FC), defined as the proportion of each vegetation class within a pixel. FC provides a consistent representation across spatial resolutions and is widely used to describe heterogeneous landscapes (Gessner et al., 2013). FC is therefore particularly valuable for bridging different spatial scales and enabling consistent interpretation across platforms. Traditionally, FC is estimated through spectral mixture analysis, which decomposes pixel reflectance into endmembers and their abundances (Zhang and Liu, 2024). However, such approaches rely on assumptions of linear mixing and require predefined endmembers, which may be difficult to define in complex heterogeneous environments such as coastal dunes. Most models developed for fractional cover estimation are either multivariable regressions or monovariate regressions, typically relying on spectral indices, texture metrics, and structural features derived from UAV and satellite imagery. However, in many of these applications, the propagation of uncertainty from fine-scale vegetation maps to satellite-scale fractional cover estimates is not explicit. The distribution of FC values in the training set may also strongly influence the final estimation accuracy, an aspect that has only recently begun to receive explicit attention (Wang and Shi, 2025).

In parallel, statistical approaches based on Dirichlet regression have been proposed to model proportional data, avoiding transformation biases and allowing consistent interpretation of compositional variables (Douma and Weedon, 2019). More recently, neural networks with Dirichlet outputs have been proposed (Sadowski and Baldi, 2018), while evidential deep learning has shown that Dirichlet parameterization can also provide an explicit measure of predictive uncertainty (Sensoy et al., 2018). Also in remote sensing, Dirichlet-based deep models have been explored for uncertainty quantification (Gawlikowski et al., 2022).

In this study, we propose and test a data-driven upscaling framework for multi-species vegetation fractional cover. Specifically, we build upon the classification presented in Belcore et al. (2024), using UAV-derived species maps as reference data to train a Dirichlet probabilistic model based on PlanetScope imagery. The approach is tested in a complex coastal dune environment characterized by high spatial heterogeneity and vegetation spectral overlap, but with a non-vegetated background (sand). By working in such a challenging setting, we aim to explore the limits of UAV-to-satellite upscaling and assess the potential of probabilistic models for large-scale small species-level vegetation mapping.

2. Materials and Methods

2.1 Study Area

The study area is located along the Tyrrhenian coast in Italy, extending approximately 20 km within the San Rossore-Massaciuccoli Regional Natural Park, a protected regional area in the Tuscany region (Figure 1). Moving from inland towards the coastline, the area transitions from Mediterranean forests, predominantly composed of pine trees, to sandy dunes stabilised by shrub and herbaceous vegetation. This vegetation community extends between 50m and 100m in width from the seashore to inland.

The interface between sea and sand is dynamic, influenced by tidal movements and storm events, which periodically deposit woody debris along the dune boundaries. These debris accumulations sometimes form structures capable of trapping sand, providing suitable substrates for pioneer vegetation species (Demichele et al., 2025). A designated portion of the park is restricted from recreational tourism, thereby creating unique conditions for studying ecosystem dynamics and the natural evolution of sandy dunes without anthropogenic interference.

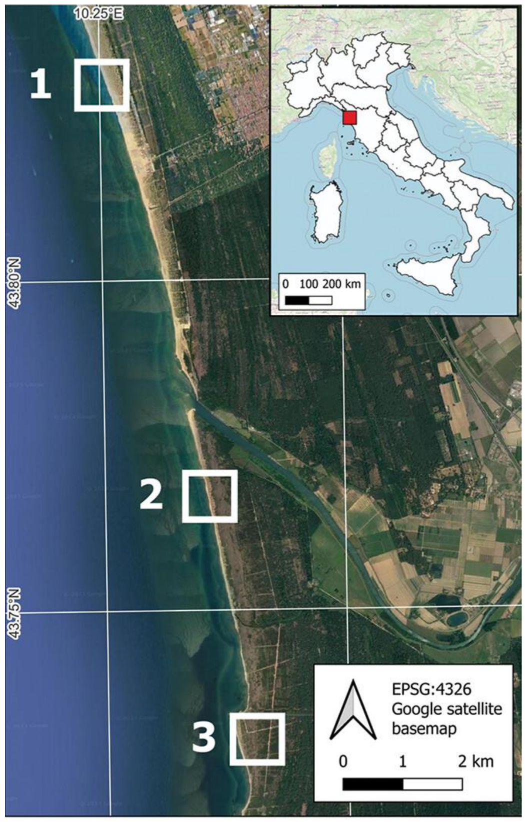

Figure 1. The three study areas along the Park area. Area 1 and Area 3 limit the satellite dataset extent (modified from Belcore et al., 2024). Google satellite background ©

2.2 Data collection

Field data for the study sites were collected at the peak growing season in mid-May and the dry season in September 2021, and both were used to build the classification dataset, to take advantage of phenological differences. Three case study areas were selected: one accessible to tourism and two with restricted access, each spanning approximately 250 m along the coastline and extending 200 m inland. In September 2021 and May 2022, two integrated geomatic surveys were carried out using multispectral optical sensors mounted on a UAV platform, DJI Phantom 4 Multispectral. Acquired imagery was processed through Structure-from-Motion (SfM) technique to produce high-resolution RGB and multispectral orthomosaics with a spatial resolution of 3 cm. The multispectral imagery comprises five spectral bands (Table 1). The detailed methodology is described in (Belcore et al., 2024).

The dataset was utilized by (Belcore et al., 2024) to construct a vegetation cover classification model employing a Random Forest classifier trained on 1,000 vegetation samples manually collected in the field using dual-frequency GNSS geodetic receivers during September 2021 and May 2022. The resulting classification achieved an accuracy of 0.76 and an F1 score ranging between 0.42 and 0.86 across 14 classes (12 species, 2 service classes), providing the basis for subsequent upscaling analyses, as shown in Figure 2. In the building of the neural network model, classes ‘Det’ (debris) and ‘Sab’ (sand) were merged (Figure 2), and the elements of the classification smaller than 5 pixels were sieved out.

Figure 2. Mapped vegetation species.

Satellite datasets from PlanetScope were also employed. PlanetScope imagery consists of nanosatellite-derived orthorectified, calibrated surface reflectance data (product 3B level, PlanetScope Ortho Analytic 8B SR), with a spatial resolution of 3 meters, captured on 23/09/2021.

Data source	Acquisition date dd/mm/yyyy	Spatial resolution [m]	Spectral resolution [nm]
UAV	23/09/2021 - 25/09/2021	0.03	*5 bands* Red (650nm ± 16nm) Green (560nm ± 16nm) Blue (450nm ± 16nm) Rededge (730nm ± 16nm) NIR (840nm ±26 nm)
Planet Scope	23/09/2021	3	*8 bands* CoastalBlue (443nm ± 10 nm) Blue (490nm ± 25nm) Green I (531nm ± 18nm) Green (565nm ± 18nm) Yellow (610nm ± 10nm) Red (665nm ± 15.5nm) Red Edge (705nm ± 7.5nm) NIR(865nm ± 20nm)

Table 1. Characteristics of the satellite and UAV datasets.

2.3 Preprocessing: Images co-registration

An initial assessment of georeferencing accuracy and spatial alignment between UAV and satellite imagery was performed. A preliminary visual inspection revealed a spatial misalignment between the UAV and PlanetScope imagery. Because such an offset could compromise pixel-level comparison and the derivation of reliable reference data, the PlanetScope data was co-registered to the UAV dataset through a Helmert transformation, assuming no scale variation between the two images. The transformation was defined as:

$$\begin{bmatrix} x' \\ y' \end{bmatrix} = \begin{bmatrix} \cos\theta & -\sin\theta \\ \sin\theta & \cos\theta \end{bmatrix} \begin{bmatrix} x \\ y \end{bmatrix} + \begin{bmatrix} t_x \\ t_y \end{bmatrix} \quad (1)$$

where:

x, y are the original PlanetScope coordinates,
x’, y’ are the transformed coordinates,
θ is the rotation angle,
t_x and t_y are the translation parameters

Six clearly identifiable control points were manually selected in both datasets for each study area, using stable objects visible in the scene, including the centroid of a white water tank and distinct shrub formations.

3. Methods

Figure 3 shows the general structure of the model. The workflow is based on the computation of fractional cover, followed by the construction of a model weighted according to UAV classification F1-scores, and producing an evidential output from which both fractional cover (as the mean) and uncertainty (as the distribution amplitude) are derived.

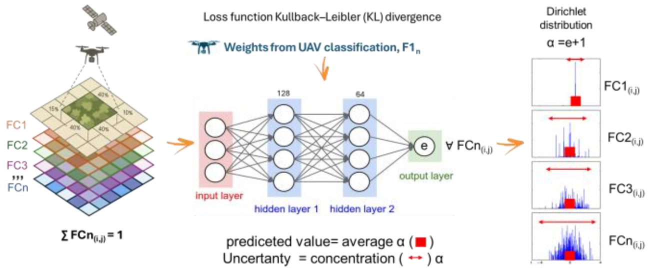

Figure 3. Structure of the upscaling analysis model.

3.1 Fractional Cover and Remote Sensing Predictors Computation

Vegetation FC was computed on a vector grid derived from PlanetScope imagery as the ratio between the area occupied by each vegetation class and the total pixel area.

$$FC_{ij} = A_i / A_{tot} \quad (2)$$

where:

FC_{ij} = represents the fractional cover of the n-th class (one for each of the 13 vegetation species, Figure 1) at pixel (i,j).
A_i = the area occupied by the vegetation class within the pixel;
A_{tot} = total area of the pixel.

Since multiple vegetation classes are present, their fractional covers of a pixel (I,j) sum up to 1.

$$\sum FCn_{(i,j)} = 1 \quad (3)$$

In cases where the sum of the fractional vegetation cover was less than 1, the remaining fraction of the pixel area was assumed to be bare soil (sand).

3.2 Spectral Consistency Across Spatial Resolutions

We first assessed whether the vegetation classes identified through UAV classification were spectrally distinguishable using the Planetscope spectral bands, assuming a reduction in spectral representativeness with decreasing spatial resolution. The spectral consistency analysis was restricted to vegetation classes explicitly represented in the UAV classification, the sand component was not included as an independent class in this analysis, since it was derived as the residual fraction required to satisfy compositional closure at the satellite pixel level (Eq. 3).

Specifically, we plotted the spectral signatures of each vegetation class, the internal variance of each class calculated for each spectral band, the number of observations (i.e., pixels) associated with each class against the NIR band standard deviation.

3.3 The regression model

For each pixel, 19 radiometric features were computed to build the training–validation–test dataset (Appendix 1).

Each pixel was transformed into a vector comprising fractional cover and spectral index values. These vectors were subsequently used as inputs for training a multi-input, multi-output regression neural network, with spectral indices as predictors and fractional covers as target variables. The predictors are listed in Appendix 1. A regression model was then developed to simultaneously estimate 13 dependent variables (the fractional covers) from 19 independent variables (the spectral features). As this is a multivariable, multi-output problem that must satisfy the constraint in Eq. (3), an approach integrating three components (Figure 3) was adopted: (i) a neural network serving as a multivariable regression model; (ii) a compositional constraint implemented through a Dirichlet distribution (Douma and Weedon, 2019; Wang and Shi, 2025); (iii) a probabilistic interpretation of predictions in terms of evidence and uncertainty.

The MLP neural network developed has a feed-forward architecture comprising two fully connected hidden layers (128 and 64 neurons) with ReLU activation and dropout. The network output was interpreted probabilistically: instead of providing a single deterministic estimate, the model produces a Dirichlet distribution for each fractional cover, i.e., a probability distribution describing how confident the model is in each prediction.
Specifically, the output layer generates a vector of non-negative evidences (e) for the vegetation fractional covers, which are then transformed into the parameters α of the Dirichlet distribution (α=e+1).α represents the probability distribution of each species within the pixel. The predicted fractional cover corresponds to the mean of the Dirichlet distribution, i.e., the most probable composition, while the spread of the distribution α expresses predictive certainty. Thus, for each pixel, the model provides both the most probable composition, with Eq. 3 satisfied, and its associated uncertainty. High evidence values generate narrow distributions around the mean (high confidence), whereas low evidence values yield broader distributions (low confidence), highlighting species or areas characterized by higher uncertainty. The loss function is a Kullback–Leibler (KL) divergence (Cui et al., 2025). The loss minimizes the KL divergence between the Dirichlet distribution predicted by the model and a target Dirichlet distribution, constructed from the observed fractional covers and weighted by the F1-scores of each species as reported by Belcore et al. (2024). Through this formulation, species with higher classification reliability contribute more strongly to the loss, while less reliable species contribute proportionally less. The loss, therefore, penalizes discrepancies between the predicted and target distributions, calibrating the model according to both label reliability and compositional structure.

3.4 Validation and large-scale application

To avoid spatial bias and overfitting, evaluation followed a Leave-One-Area-Out (LOAO) strategy across three cycles, where one area served as validation and the remaining two as training. For each training cycle, internal testing employed spatial GroupKFold cross-validation (5 blocks of 60 m × 60 m) to prevent spatial bias due to adjacent zones. The validation scheme is shown in Figure 4. Additive Gaussian noise, proportional to the standard deviation of spectral features, was used as data augmentation to simulate intra-class radiometric variability and improve generalization. Macro-level and per-species RMSE and MAE were computed.

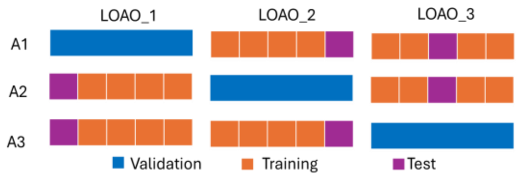

Figure 4. Validation scheme. A*n* = the study Area, LOAO_*n*= Leave-One-Area-Out cycle.

4. Results

4.1 Preprocessing: Image co-registration

The PlanetScope Ortho Scene product has a declared nominal positional accuracy of 10 m RMSE (90th percentile). Independent assessments further indicate that relative geolocation accuracy is typically on the order of 4 m, although it may vary depending on acquisition conditions and geographic context. By contrast, the UAV dataset, georeferenced using GNSS RTK, achieved an average horizontal accuracy of approximately 2 cm.
Given this difference in positional accuracy, the UAV imagery was retained as the geometric reference, and the PlanetScope dataset was co-registered to it through a scale-fixed Helmert transformation. The co-registration was based on six clearly identifiable ground control points distributed across the study area. The final alignment resulted in a Mean Error of 2,30 m, which is lower than the PlanetScope pixel size. This indicates that residual geometric discrepancies are negligible with respect to the spatial resolution of the satellite data and are therefore unlikely to significantly affect subsequent analyses. Nevertheless, it was necessary to ensure reliable pixel-level comparison between datasets.

4.2 Spectral Consistency Across Spatial Resolutions

The analysis of spectral signatures (Figure 5) shows a highly consistent trend across all classes, particularly for herbaceous species. Only slight deviations are observed for shrub and arboreal species, such *Pinus*, *Juniperus* and *Yucca*; however, the main discriminating factor appears to be the overall reflectance intensity rather than the spectral pattern itself. This behaviour is expected, as the analysis is restricted to vegetation classes with broadly similar spectral responses, especially in the visible and near-infrared domains.
While differences in signal intensity could be sufficient to discriminate among species, this is only effective when intra-class variability remains limited. The boxplots in Figure 7 highlight that this condition is not always satisfied. Some species, such as *Pancratium* and *Yucca*, exhibit wide distributions of reflectace and a large number of outliers, indicating substantial intra-class variability. This is particularly evident for species such as *Yucca*, where the spread of values across bands suggests strong heterogeneity in spectral response at satellite scale. This variability is likely related to small patch size, mixed pixels, and local environmental conditions affecting reflectance.
A further important aspect concerns the relationship between sample size and intra-class variability (Figure 6) since species that combine a limited number of available samples with high

internal variability have a reduced reliability of their spectral characterization. This is the case, for example, for *Yucca* and, to a lesser extent, *Pancratium* and *Achillea*, where both low sample support and high variability contribute to increased uncertainty in the spectral domain.

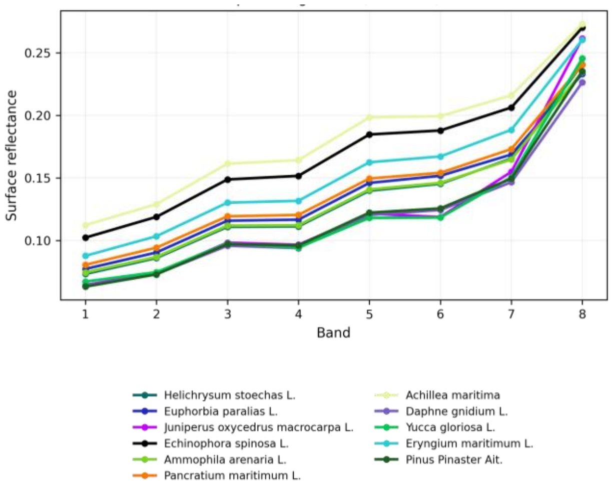

Figure 5. Spectral signatures from PlantScope data, comuted as average surface reflectance on pixels with Franctional Cover (FC) ≥10

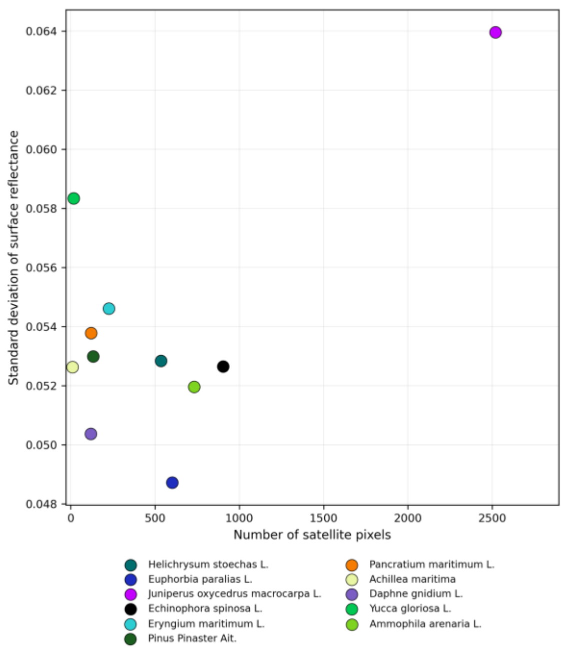

Figure 6. Relationship between abundance in satellite pixels and internal variance of the analysed species (NIR band)

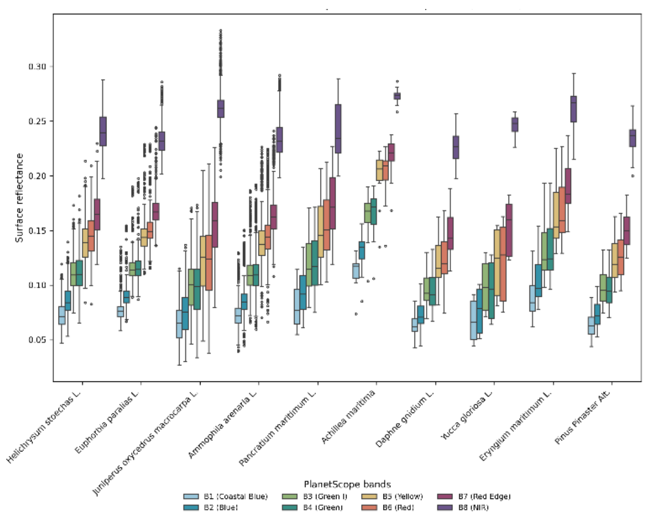

Figure 7. Variance of UAV-detected classes in PlanetScope bands

4.3 The regression model

The evidential-Dirichlet model yielded consistent results across the three LOAO cycles, showing macro-MAE = 0.09, 0.08, and 0.11 for Area 1, 2, and 3, respectively, and macro-RMSE = 0.11, 0.11, and 0.13, which corresponds to an absolute error of 9–13% in fractional covers. The internal cross-validation produced a macro-RMSE of 0.107 ± 0.003, confirming the model stability. As shown in Figure 8, the lowest errors (MAE) were observed for psammophilous forbs and succulents (*Eryngium maritimum*, *Euphorbia paralias*, *Achillea maritima*, *Echinophora spinosa*, *Helichrysum stoechas*), with MAE values below 0.08. Woody and arboreal species (*Pinus pinaster*, *Juniperus macrocarpa)* showed higher errors, with MAE reaching 0.35 and RMSE ranging from 0.16 to 0.20 (Table 2), likely related to canopy structural complexity and greater intra-class radiometric variability.
The background sand class exhibited the highest uncertainty (RMSE 0.41), revealing a heterogeneous spectral response.

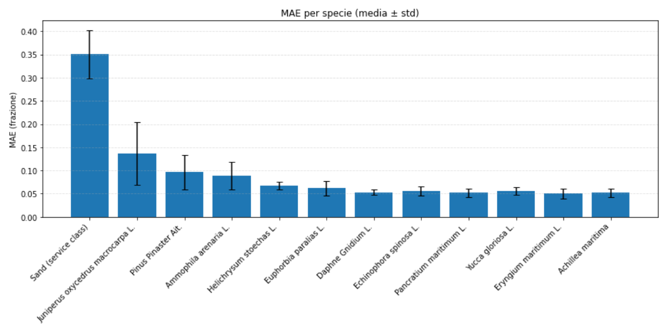

Figure 8. Macro-Mean Absolute Error (MAE) of the examined classes and corresponding standard deviation

A relevant limitation of the proposed framework concerns rare species, i.e., classes characterized by low fractional cover and spatially sparsely distributed in the reference dataset. Under these conditions, performance assessment becomes intrinsically difficult, as standard error metrics may be strongly influenced by the predominance of near-zero values or by a very limited number of positive observations. Near-zero values are frequent due to the nature of the evidential-Dirichlet, which predictions are never equal to zero. As a result, species with very low

https://doi.org/10.5194/isprs-archives-XLIX-B3-2026-897-2026 | © Author(s) 2026. CC BY 4.0 License.

occurrence may show low absolute errors when evaluated across all pixels, while remaining difficult to model under actual presence conditions.

To better account for this effect, a threshold-based correction was introduced in addition to the standard RMSE. Specifically, an abundance-constrained metric, referred to as RMSE*, was computed by considering only pixels where the observed fractional cover exceeded a minimum threshold, set to 0.05 (FC>0.05). The abundance-corrected metrics are reported in Table 2.

Species	Macro RMSE	SD	RMSE *	P	RP	frac_ RP
Sand	0.404	0.048	0.410	0.628	4087	0.962
Juniperus	0.209	0.131	0.389	0.081	1156	0.189
Pinus	0.161	0.072	0.458	0.035	387	0.122
Ammophila	0.131	0.065	0.180	0.081	1001	0.359
Helichrysum	0.094	0.026	0.109	0.059	972	0.317
Euphorbia	0.072	0.030	0.088	0.028	415	0.199
Daphne	0.063	0.011	0.102	0.019	391	0.132
Echinophora	0.059	0.004	0.078	0.020	710	0.095
Pancratium	0.056	0.011	0.090	0.008	159	0.045
Yucca	0.055	0.007	0.132	0.001	13	0.003
Achillea	0.055	0.009	0.045	0.002	29	0.004
Eryngium	0.051	0.006	0.046	0.011	325	0.079

Table 2. Model validation results. Macro RMSE in the mean RMSE of the three LOAO cycles; SD is the standard deviation of LOAO cycles; RMSE* is the RMSE calculated on the test pixel with FC >0.05; Presence (P) of the species in the test set in 0-1; Real Presence (RP) is the number of pixel in which the species FC is >0.05; Fractional Real Presence (frac_RP) is the fraction of test pixel, computed as RP on P.

4.4 Validation and large-scale application

The trained model was applied to the entire study area. To obtain a more interpretable output and reduce the effect of very low, non-informative predictions, all values below a threshold of 0.05 were set to zero and reassigned to an "other species" class in a post-processing step.

Figure 9 shows the spatial distribution of *Ammophila arenaria*, one of the key species colonizing dune crests, together with elevation contours derived from UAV data. From visual interpretation, a clear correspondence can be observed between areas of high Ammophila cover and dune crest positions, supporting the consistency of the model output at landscape scale.

5. Discussion

In UAV-to-satellite upscaling of species-level vegetation classification, one of the main difficulties is the change of spatial resolution between datasets and the consequent spectral mixing. Indeed, the transition from centimetric UAV observations to metre-scale satellite pixels increases the spectral mixing and raises the risk of propagating classification errors from the UAV reference layer to the satellite-scale prediction. On the other hand, the augmented spectral resolution of satellites might compensate for the reduced spatial resolution, enabling a data-driven spectral unmixing. In this study, we attempt to address these issues by adopting a fractional cover framework coupled with a probabilistic model that explicitly takes into consideration the reliability of the input classification.

Figure 9. Plotting of FC >10 of *Ammophila arenaria* cover and the foredune crestline as identified in (Demichele et al., 2025). Area 2, EPSG: 32632

Considering the discrepancy between spatial resolutions, the spectral signatures reported in Figure 5 must be interpreted with caution. Although they are associated with classes mapped at 3 cm, the corresponding satellite values are extracted from mixed pixels. As a consequence, the smaller or more spatially fragmented the species, the less representative its spectral signature becomes. This is a common spectral mixing condition; indeed, it is evident from Figure 5 that small species with discontinuous cover, such as *Achillea* and *Echinophora*, show very similar spectral responses at the satellite scale, whereas more spatially continuous formations, such as dense *Ammophila arenaria* stands, maintain a more coherent signal. This is also confirmed by the boxplots in Figure 7, where the species with the strongest overlap among spectral distributions also show the largest internal variability. These patterns highlight the difficulty of representing fine ecological heterogeneity at broader spatial resolutions, reinforcing the need to work with fractional cover rather than hard class transfer, assuming that the mixed spectral response of each pixel can be interpreted as the combination of multiple vegetation components. The need for a composite approach, such as the fractional cover, is especially relevant in coastal dune systems, where vegetation is rarely distributed in large homogeneous patches and where species associations are controlled by common geomorphological and environmental constraints.

The model performances indicate a stable model behaviour across the three test areas. As shown by the Standard Deviation (SD) in Table 2, the relative ranking of species errors remains broadly consistent in A1, A2, and A3, suggesting a good spatial generalization and the capability of the model to capture spectral-structural patterns rather than area-specific effects only. The lowest errors were observed for psammophilous forbs and succulents, including *Eryngium maritimum*, *Euphorbia paralias*, *Achillea maritima*, *Echinophora spinosa*, and *Helichrysum stoechas*. Woody and arboreal species, specifically *Pinus pinaster* and *Juniperus oxycedrus*, showed the highest errors (Table 2), with average RMSE values reaching 0.40±0.048. This behaviour is plausibly related to canopy structural complexity, shadow effects, and higher intra-class radiometric variability. Although a first sign appears as promising results, a more cautious interpretation is required for species with low overall RMSE but very limited spatial presence, such as *Yucca*, *Achillea,* and *Eryngium*. The additional analysis reported in Table 2 shows that these species are only apparently accurately detected; in fact, they are rare classes, for which low global errors are partly driven by the predominance of near-zero pixels. Indeed, the RMSE*, although still relatively low, can be larger than the species' fractional presence, like for *Yucca*. In these cases, the apparent accuracy can be linked to species rarity, whereas the error on present pixels reveals the actual difficulty of modelling these taxa.

Different conditions are registered for more abundant species, such as *Pinus pinaster*, whose global RMSE remains moderate, while the error calculated only on pixels with observed presence above threshold (RMSE*) increases markedly. A similar behaviour is observed for *Juniperus*. This behavior supports the hypothesis that for woody species, the main limitation is not only low frequency but also their structural and spatial complexity at satellite resolution.

The sand background class remains the most problematic component of the model; its RMSE and RMSE* are both high and very similar, which is expected given its broad spatial extent and high abundance. In this case, model difficulty does not arise from rarity but from strong internal heterogeneity. In fact, it groups together not only bare sand but also detrital material (as per Figure 2), woody debris, less than 5 UAV-pixel vegetation, and, in some cases, anthropogenic residues. The transitional areas between bare sediment and vegetation further increase spectral ambiguity, which explains the persistent error associated with this class. The "background" label is therefore only a practical simplification, which calls for further investigation.

Overall, the rare species, showing low Presence values, remain the main limitations of multi-species fractional cover upscaling. Some taxa, such as *Yucca gloriosa*, show low global RMSE values but extremely low Presence and fractional presence (0,003), and their error increases substantially when evaluation is restricted to pixels where the species is actually present. This reflects the fact that a low global error may simply result from the prevalence of absence conditions. From an ecological point of view, this aspect limits the identification of isolated specimens, which may be of great ecological importance, either as indicators of ecosystem health or, as in the case of *Yucca*, as invasive species that are rapidly spreading throughout the area. By contrast, species such as *Helichrysum, Echinophora*, and *Euphorbia* maintain relatively low RMSE* values, indicating that, despite their small size and fragmented distribution, their prediction remains comparatively robust under actual presence conditions, suggesting that the rarity alone does not fully explain model performance and that the spatial organization and spectral coherence also play an important role.

From a methodological point of view, the Dirichlet-based formulation guarantees compositional consistency in a problem where all fractional covers must sum to one. This is a relevant advantage over approaches that impose normalization a posteriori or rely on independent outputs that may violate or force the closure constraint, such as the Softmax function. A further advantage is the possibility of deriving an uncertainty estimation with the prediction itself. This additional information is particularly valuable in ecologically complex systems, where mixed pixels, rare species, and transition zones make interpretation intrinsically uncertain. In this sense, the model does not provide only a map of predicted cover, but also a spatially explicit indication of where those predictions should be interpreted more cautiously (Figure 9).

The large-scale application confirms that the model captures meaningful vegetation patterns beyond the training patches. In particular, the predicted distribution of *Ammophila arenaria* along the dune belt appears spatially coherent with the main geomorphological gradients and with the expected vegetation arrangement within the park. This is proof that the model output can also provide useful proxy information on vegetation structure at the landscape scale. However, there is still considerable room for improvement in the handling of rare species and the background class, which was simplified in this application, as well as in the model's generalization. Indeed, transferability remains the major limitation of this application. While the model has shown encouraging spatial generalization under LOAO validation, it has not yet been tested under temporal transfer. This is a crucial aspect, since phenological variability may alter species separability and therefore affect the stability of the upscaling relationship. Future work should therefore focus on temporal robustness, on increasing the representation of rare species, and, where necessary, on the aggregation of ecologically similar taxa when the available support is insufficient.

6. Conclusion

Overall, results demonstrate that the fractional cover model, while accounting for label uncertainty, enables stable UAV-to-satellite upscaling. Despite the challenging application, this approach demonstrates strong potential for bridging the gap between local UAV data and satellite observations for multi-scale vegetation mapping. Further analyses will investigate temporal transferability, intra-class variability, and fractional-cover aggregation strategies.

Acknowledgements

We would like to thank the people who participated in the field activities in 2021, in particular UAV-pilot Paolo Maschio, Prof. Carlo Camporeale, and PhD Melissa Latella. We would also like to thank the Migliarino, Massaccicoli, and San Rossore Park Authority in Pisa, Italy for hosting these research activities.

References

Agrillo, E., Filipponi, F., Salvati, R., Pezzarossa, A., Casella, L., 2023. Modeling approach for coastal dune habitat detection on coastal ecosystems combining very high-resolution UAV imagery and field survey. Remote Sens. Ecol. Conserv. 9, 251–267. https://doi.org/10.1002/rse2.308

Alvarez-Vanhard, E., Corpetti, T., Houet, T., 2021. UAV & satellite synergies for optical remote sensing applications: A literature review. Sci. Remote Sens. 3, 100019. https://doi.org/10.1016/j.srs.2021.100019

Belcore, E., Latella, M., Piras, M., Camporeale, C., 2024. Enhancing precision in coastal dunes vegetation mapping: ultra-high resolution hierarchical classification at the individual plant level. Int. J. Remote Sens. 45, 4527–4552. https://doi.org/10.1080/01431161.2024.2354135

Cui, J., Zhu, B., Xu, Q., Tian, Z., Qi, X., Yu, B., Zhang, H., Hong, R., 2025. Generalized Kullback-Leibler Divergence Loss. https://doi.org/10.48550/ARXIV.2503.08038

Demichele, D., Belcore, E., Piras, M., Camporeale, C., 2025. Species-By-Species Pattern Analysis of Coastal Dune Vegetation. J. Geophys. Res. Biogeosciences 130, e2024JG008419. https://doi.org/10.1029/2024JG008419

Demichele, D., Belcore, E., Piras, M., Camporeale, C., 2025. Species-By-Species Pattern Analysis of Coastal Dune Vegetation. J. Geophys. Res. Biogeosciences 130, e2024JG008419. https://doi.org/10.1029/2024JG008419

Douma, J.C., Weedon, J.T., 2019. Analysing continuous proportions in ecology and evolution: A practical introduction to beta and Dirichlet regression. Methods Ecol. Evol. 10, 1412–1430. https://doi.org/10.1111/2041-210X.13234

Gawlikowski, J., Saha, S., Kruspe, A., Zhu, X.X., 2022. An Advanced Dirichlet Prior Network for Out-of-Distribution Detection in Remote Sensing. IEEE Trans. Geosci. Remote Sens. 60, 1–19. https://doi.org/10.1109/TGRS.2022.3140324

Gessner, U., Machwitz, M., Conrad, C., Dech, S., 2013. Estimating the fractional cover of growth forms and bare surface in savannas. A multi-resolution approach based on regression tree ensembles. Remote Sens. Environ. 129, 90–102. https://doi.org/10.1016/j.rse.2012.10.026

Karakizi, C., Okujeni, A., Sofikiti, E., Tsironis, V., Psalta, A., Karantzalos, K., Hostert, P., Symeonakis, E., 2024. Mapping savannah woody vegetation at the species level with multispecral drone and hyperspectral EnMAP data. https://doi.org/10.48550/ARXIV.2407.11404

Kattenborn, T., Eichel, J., Wiser, S., Burrows, L., Fassnacht, F.E., Schmidtlein, S., 2020. Convolutional Neural Networks accurately predict cover fractions of plant species and communities in Unmanned Aerial Vehicle imagery. Remote Sens. Ecol. Conserv. 6, 472–486. https://doi.org/10.1002/rse2.146

Leitão, P.J., Schwieder, M., Pedroni, F., Sanchez, M., Pinto, J.R.R., Maracahipes, L., Bustamante, M., Hostert, P., 2019. Mapping woody plant community turnover with space-borne hyperspectral data – a case study in the Cerrado. Remote Sens. Ecol. Conserv. 5, 107–115. https://doi.org/10.1002/rse2.91

Nasiri, V., Darvishsefat, A.A., Arefi, H., Griess, V.C., Sadeghi, S.M.M., Borz, S.A., 2022. Modeling Forest Canopy Cover: A Synergistic Use of Sentinel-2, Aerial Photogrammetry Data, and Machine Learning. Remote Sens. 14, 1453. https://doi.org/10.3390/rs14061453

Paz-Kagan, T., Silver, M., Panov, N., Karnieli, A., 2019. Multispectral Approach for Identifying Invasive Plant Species Based on Flowering Phenology Characteristics. Remote Sens. 11, 953. https://doi.org/10.3390/rs11080953

Räsänen, A., Juutinen, S., Tuittila, E.-S., Aurela, M., Virtanen, T., 2019. Comparing ultra-high spatial resolution remote-sensing methods in mapping peatland vegetation. J. Veg. Sci. 30, 1016–1026. https://doi.org/10.1111/jvs.12769

Sadowski, P., Baldi, P., 2018. Neural Network Regression with Beta, Dirichlet, and Dirichlet-Multinomial Outputs.

Schiefer, F., Schmidtlein, S., Frick, A., Frey, J., Klinke, R., Zielewska-Büttner, K., Junttila, S., Uhl, A., Kattenborn, T., 2023. UAV-based reference data for the prediction of fractional cover of standing deadwood from Sentinel time series. ISPRS Open J. Photogramm. Remote Sens. 8, 100034. https://doi.org/10.1016/j.ophoto.2023.100034

Sensoy, M., Kaplan, L., Kandemir, M., 2018. Evidential Deep Learning to Quantify Classification Uncertainty. https://doi.org/10.48550/arXiv.1806.01768

Villoslada, M., Berner, L.T., Juutinen, S., Ylänne, H., Kumpula, T., 2024. Upscaling vascular aboveground biomass and topsoil moisture of subarctic fens from Unoccupied Aerial Vehicles (UAVs) to satellite level. Sci. Total Environ. 933, 173049. https://doi.org/10.1016/j.scitotenv.2024.173049

Wang, R., Shi, C., 2025. The impact of fractional cover distribution in training samples on the accuracy of fractional cover estimation: a model-based evaluation. Geo-Spat. Inf. Sci. 0, 1–39. https://doi.org/10.1080/10095020.2025.2514815

Yamati, F.R.I., Heim, R.H., Günder, M., Gajda, W., Mahlein, A.-K., 2023. Image-to-image translation for satellite and UAV remote sensing: a use case for Cercospora Leaf Spot monitoring on sugar beet., in: 2023 IEEE International Workshop on Metrology for Agriculture and Forestry (MetroAgriFor). Presented at the 2023 IEEE International Workshop on Metrology for Agriculture and Forestry (MetroAgriFor), pp. 783–787. https://doi.org/10.1109/MetroAgriFor58484.2023.10424276

Zhang, T., Liu, D., 2024. Estimating fractional vegetation cover from multispectral unmixing modeled with local endmember variability and spatial contextual information. ISPRS J. Photogramm. Remote Sens. 209, 481–499. https://doi.org/10.1016/j.isprsjprs.2024.02.018

Appendix

Name (Acronym)	Formula
NDVI (Normalized Difference Vegetation Index)	(NIR - Red) / (NIR + Red)
IPVI (Infrared Percentage Vegetation Index)	NIR / (NIR + Red)
NDBI (Normalized Difference Built-up Index)	(SWIR - NIR) / (SWIR + NIR)
SR (Simple Ratio)	NIR / Red
LAI (Leaf Area Index)	Empirical relationship with NDVI or EVI
EVI (Enhanced Vegetation Index)	2.5 × (NIR - Red) / (NIR + 6×Red - 7.5×Blue + 1)

ARVI (Atmospherically Resistant Vegetation Index)	(NIR - (2×Red - Blue)) / (NIR + (2×Red - Blue))
GNDVI (Green Normalized Difference Vegetation Index)	(NIR - Green) / (NIR + Green)
GRVI (Green-Red Vegetation Index)	(Green - Red) / (Green + Red)
SAVI (Soil Adjusted Vegetation Index)	(1 + L)(NIR - Red) / (NIR + Red + L), L = 0.5
MSAVI2 (Modified Soil Adjusted Vegetation Index)	$[2\times NIR + 1 - \sqrt{(2\times NIR + 1)^2 - 8\times(NIR - Red)}]/2$
NDWI (Normalized Difference Water Index)	(NIR - SWIR) / (NIR + SWIR)
Brightness Index	$\sqrt{Red^2 + Green^2}$ or derived from PCA of bands
VARI (Visible Atmospherically Resistant Index)	(Green - Red) / (Green + Red - Blue)
MCARI (Modified Chlorophyll Absorption Ratio Index)	[(RedEdge - Red) - 0.2×(RedEdge - Green)] × (RedEdge / Red)
NDRE (Normalized Difference Red Edge)	(NIR - RedEdge) / (NIR + RedEdge)
MRENDVI (Modified Red-Edge NDVI)	(NIR - RedEdge) / (NIR + Red)
TCARI (Transformed Chlorophyll Absorption Reflectance Index)	3×[(RedEdge - Red) - 0.2×(RedEdge - Green)×(RedEdge / Red)]
PSRI (Plant Senescence Reflectance Index)	(Red - Blue) / RedEdge

https://doi.org/10.5194/isprs-archives-XLIX-B3-2026-897-2026 | © Author(s) 2026. CC BY 4.0 License.